July 29, 2016

Kevin Lalli

OPTI575: Professional Paper

Prototype Development of a Space Qualified MWIR Imager

Abstract

This paper documents the instrument goals, optical design, and test plan of a prototype MWIR thermal imager to be qualified under flight-like environments. The prototype design has been completed and is presented. Performance goals, design philosophy, resultant design and environmental plans are covered.

Part I: Business Context & Design Goals

Planetary Resources, Inc. (PRI) is poised to launch a constellation of small satellites, beginning in 2017, for earth observation in the 3-5 micron midwave infrared (MWIR) band for thermal imaging. The near-term goal is to provide actionable data to customers such as commercial agriculture, oil and gas, and financial forecasting[1]. The instrument and control systems technology feeds forward to the company's long-term objective to prospect and mine asteroids for water and mineral components[2]. One of the drivers in choosing the MWIR band was utility for identifying hydrated minerals, which have strong absorption features in the band[2,3].

The Arkyd-100 (A100) series of satellites will comprise the earth observation constellation, and will likely be bifurcated by MWIR- and hyperspectral-specific models of satellite. At the beginning of 2016, plans were made to fly a prototype instrument in family with the constellation MWIR instrument design. Since one of the biggest roadblocks for a commercial satellite company is the cost and availability of launch opportunities, PRI decided to go with a form-factor that would maximize opportunities across various launch vehicles. This led to high-level design goal of Cubesat compatibility.

By definition, Cubesats are small satellites that follow a form factor standard defined by 10 cm x 10 cm x 10 cm units. The CubeSat definition was originally developed by California Polytechnic State University[4], and has been increasingly adopted by commercial providers for secondary payloads[5,6,7], as well as commercial satellite missions[8]. A twelve-unit (12U) Cubesat allows for 20 cm x 20 cm x 30 cm dimensions, which dictate restrictions on track length, volume, and aperture dimensions defined in the next section.

Unfortunately, external delays of launch schedule and shifts in internal priorities meant that an A100 pathfinder was not possible until later in 2017. Instead, two 6-unit Arkyd-6 (A6) satellites, which are completed and scheduled for launch, will serve to de-risk the communication and data systems, and include a proof-of-concept instrument at reduced resolution. In place of launching an A100 pathfinder immediately, a ground prototype instrument is to be assembled and tested in the fourth quarter of 2016 will maintain a 12U-compatible form factor and all other flight requirements. Volume and weight are always significant launch considerations, so maintaining these goal is relevant to an intermediate pathfinder launch as well as forthcoming constellation satellites.

The re-scoped A100 instrument prototype maintains many of the same design goals, but validation efforts are focused on ground testing rather than launch preparation. While it is impossible to simulate the exact conditions of launch and space environment, equally valuable lessons will be learned on the ground through imaging performance and representative environmental testing.

Part II: Optical Design

A. System Requirements

The 12U cubesat compatibility dictates the spacecraft form factor, which imposes subsequent requirements on the instrument. Additionally, the launch availability for secondary payloads using Cubesat compatible launch interfaces led to a notional orbital altitude (h) of 550 kilometers.

A driving philosophy of PRI is to bring as much fabrication and design as possible. However, at this stage it was determined that a commercially available integrated detector and cryocooler assembly (IDCA*) was preferred to developing a custom camera core. For the A6 instrument and A100 prototype effort, a commercial IDCA based on

a 520 x 612 indium antimonide (InSb) detector was selected primarily for on size weight and power advantages over competing options.

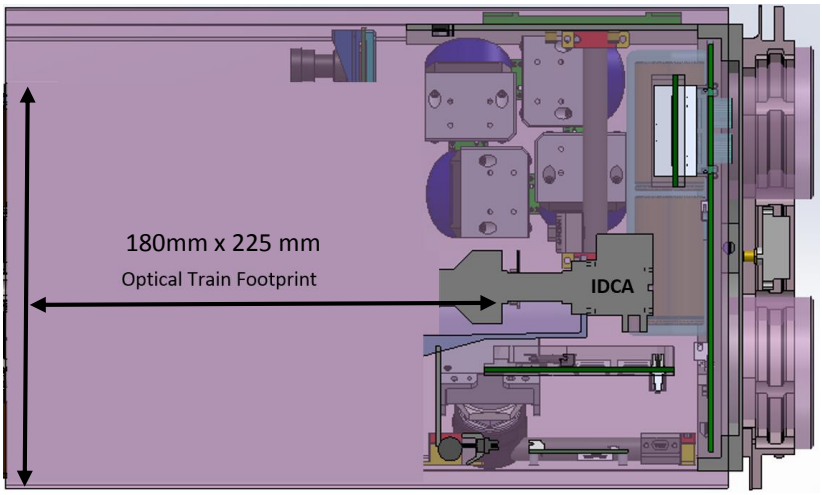

The conceptual 12U spacecraft architecture is shown, including avionics stacks, reaction wheels, star trackers, and the instrument IDCA. The vertical dimension restricts the instrument aperture, and the horizontal dimension defines the maximum track length.

As is common with cryocooled detectors, a cold stop is incorporated into the vacuum dewar ahead of the focal plane array, which consequently sets the system focal ratio to F/4. The choice of IDCA fully constrains the diffraction-limited sampling ratio Q_{DL} to 1.07, based on a 15 µm pixel pitch, f-number (F), and central wavelength of 4.0 µm.

$$Q_{DL} = \lambda * F/p$$

This metric is independent of the optical design or orbit choice. This sampling ratio is below the Nyquist-sampled value of Q = 2, but there are a number of advantages of having Q < 2. A major advantage is increased SNR per pixel, which is especially important in the context of satellite instruments for earth observation[9,10,11].

To maintain this optically-limited sampling ratio, a requirement for diffraction-limited optics was imposed as a Strehl ratio of 0.8. This a common single-metric expression of diffraction limited performance used, for example, in the design of the James Web Space Telescope[12]. This translates to 0.075 waves of polychromatic RMS wavefront error; this was the metric used for optimization and analysis. This performance requirement must be held across the operating temperature range, meaning the optical train must be athermalized.

Ground sample distance (GSD) is defined as the projection of a detector element onto the ground. For fixed pixel pitch and altitude, the minimum possible GSD is a function of only system focal length expressed as[10,13]

$$GSD_{min} = p * \frac{h}{f_{max}}$$

Based on market research in precision agriculture and mining, the business team generated an original goal of 10 meter GSD from a proposed orbital altitude of 550 km. However, being restricted by the 180 mm maximum diameter defined above, and the focal ratio of the IDCA, the maximum focal length possible is 720 mm. The resultant minimum GSD of 11.5 meters still gives resolution well above those currently available in the 3-5 µm bandpass and was deemed a sensible compromise at the prototype stage.

The IDCA cold stop geometry, window element, and additional cold filter were incorporated into the optical design early on. This was critical for maximizing cold stop efficiency[14], as well as correcting for focal shift and color effects of the transmissive elements. Geometric system throughput, defined as the combined effects of obscuration and vingetting at the cold stop, was required to be above 80% in the center of the field, and 70% at full-field. This does not account for coating transmission or reflective losses.

Notional spacecraft and orbital parameters, and key detector specifications are listed in the table below. These flow down to system requirements to inform the optical design.

Spacecraft & Orbital Parameters		IDCA Specifications	
Spacecraft Length	30 cm	Cold Stop Diameter	4.832 mm
Spacecraft Width, Height	20 cm	Cold Stop – FPA Distance	19.33 mm
Orbital Altitude	550 km	Focal Ratio	F/4
Operating Temperature Range	-40° C – 60° C	Pixel Pitch	15 µm
Non-op Temperature Range	-100° – 120° C	Dimensions	640 (H) x 512 (V)
Vibration Test Environment	GEVS[15]	Sampling Ratio (Q_{DL})	1.07

Optical System Requirements	
Focal Ratio	F/4
Max Diameter	180 mm
Max Track Length	225 mm
Focal Length	720 mm
Field of View	0.98°
Image Performance	Strehl ≥ 0.8 (Diffraction-limited)
Geometric Throughput	80% center, 70% full-field

The performance requirements of the prototype are capability driven, rather than being set with a specific application in mind. While exact application goals were not imposed at this stage, the ability to separate solar reflectance (3-4.2 µm) from thermal emissions (4.5 µm and above) is desirable. Because of this, a final design requirement was to include space in collimated beam path for a spectral filter, or filter wheel. This will also enable multi-spectral imaging as a variety of applications are explored. Signal-to-noise (SNR) quantification, including modelled atmospheric effects from orbit, will be a priority through prototype development. These studies will better define traceability of measurements across a range of application scenarios.

B. Telescope Design

The instrument architecture is based around a reflective front-end telescope designed to collect and focus light to an intermediate focal plane, and set the system focal length. This also has the advantage of being able to accommodate other instruments, or a context camera imaging over visible bands. Gold-plated reflective surfaces are currently utilized for increased transmission in the MWIR.

A field-flattened Ritchey Chretien was considered as a starting point, but the restrictions imposed[16] by an aplanatic system made it difficult to maintain 12U form factor. Instead, a folded Gregorian design was utilized[17] which alleviated many of the constraints posed by track length. Another advantage of this design is that it turns the primary-secondary alignment tolerances of a traditional Gregorian into manufacturing tolerances, as the surfaces are set into a monotlithic substrate. The cited design emphasizes the importance of diamond turned surfaces to realize the monolith that includes primary and secondary surfaces. However, requiring athermalization over the operating environment led to a zero-CTE monolith design ground from Zerodur. This also places a manufacturing limit on the primary speed of F/1.1, which has implications for the telescope layout described.

The telescope focal plane was chosen to coincide with the vertex of the primary mirror, i.e. a back focal length of zero. This achieves a balance between access during alignment and a short track length, and requires the minimum necessary central hole size for improved structural stability. This is a flexible point in the design if configurational changes are needed.

Using the framework of Whetherell and Rimmer[16], the four necessary fundamental design parameters (F, Dp, Fp, and B) have been established to inform a detailed telescope layout.

$$F = -4\,;\quad D_p = 180\ mm;\quad F_p = 1.1;\ B = 0$$

Where F is taken to be negative for a Gregorian telescope due to image inversion. These parameters are used to calculate the secondary mirror magnification, and total separation from primary to secondary mirror surface:

$$m = \frac{F}{F_p} \qquad \text{(Secondary magnification)}$$

$$S = D_p * \frac{F - B/D_p}{m + 1} \qquad \text{(Primary-secondary separation)}$$

A secondary magnification of -3.6 is effectively set by the F/1.1 manufacture limit on the primary surface. The separation between primary secondary surfaces of 278 mm would be exactly twice the separation from the fold mirror, if the monolithic substrate could be manufactured with coincident surface vertices. However, a vertex-to-vertex separation (δ) of no less than 4mm was required for grinding of the secondary surface. This leads to a separation from primary vertex to fold mirror of

$$S_{fold} = (S - \delta)/2$$

Thus, the separation between primary and fold mirror is 137 mm in the first-order design. Radii of curvature for the primary and secondary are also computed by reference to the fundamental design parameters using

$$R_p = -2 * D_p * F_p \quad ; \quad R_s = 2 * m * D_p * (F_p + B/D_p)$$

This yields primary and secondary radii of 400 mm and 120.4 mm, respectively. The exit pupil location, which will be important in the following section, is located 200 mm left of the telescope focal plane, as defined by

$$l_{ep} = -m * F\,\frac{D_p\left(F_p + B/D_p\right)}{\left(m * F + B/D_p\right)}$$

For a back focal length of zero, this reduces to the focal length of the primary, i.e. half the primary radius. Since a departure from an aplanatic, field-flattened telescope introduces the need for corrective optics in any case, a parabolic primary was chosen over an elliptical one for ease of manufacture and testing. The choice of conic constant is made to correct for secondary's spherical aberration only[20].

$$K_2 = -\left(\frac{m+1}{m-1}\right)^2$$

A final note on the telescope design – the limitation on primary focal ratio increases obstruction by 24% from the minimum theoretical obstruction proposed by Dragonov (with 0.41 radial obstruction versus the minimum possible 0.33). The system geometric throughput still satisfies the greater than 80% requirement, and alternate telescope designs may be revisited for the flight instrument depending on the final spacecraft configuration and instrument SNR studies.

Telescope Layout

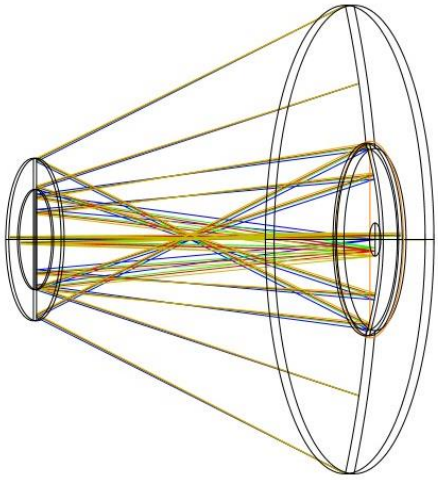

Spot Diagram

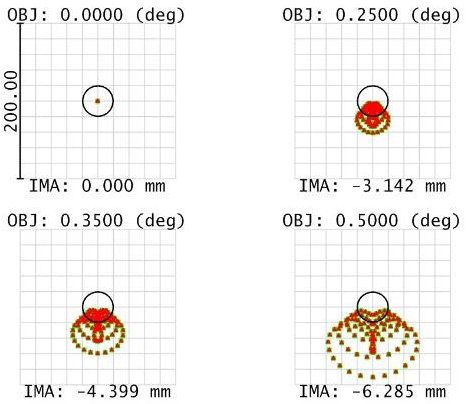

Spot sizes: 0, 21, 30, 47 µm
(Airy disk is 19.5 µm, for central 4 µm wavelength)

C. Relay Design

The back-end of the system is a 1:1 relay lens that corrects for the telescope's inherent coma and field curvature, re-images the field onto the focal plane array of the IDCA, and optimizes cold stop efficiency. This means that the relay images at two sets of conjugates: one being from the telescope focal plane to the detector, and the other from the telescope exit pupil to the cold stop (entrance pupil) of the IDCA[18]. On the object side of the relay, the telescope focal plane and exit pupil location have a fixed offset. Similarly, the detector distance (x') and reimaged pupil location (l_{ep}') are related by the IDCA cold stop to FPA distance.

$$\frac{1}{f_{rel}} = \frac{1}{x + l_{ep}} + \frac{1}{x' - l_{ep}'} = \frac{1}{x + l_{ep}} + \frac{1}{19.33\ \text{mm}}$$

To remain within the track length requirement while having adequate clearance for mechanical interfaces, object/ image distances of 41.5 mm were chosen with a corresponding relay focal length of 21 mm.

The need for a buried filter wheel means that the relay should consist of a front (collimator) and rear (camera) group, with a collimated space in the middle. Placing filters in a collimated space has some advantages[18], but especially the flexibility in space as the filter wheel design changes or grows. For the prototype instrument, a clearance of 20 mm was desired. Using this separation distance, the relay was split into two groups, collimator and camera, of equal powers for unit magnification. Taking the equation for two thin lenses of equal focal length separated by a distance t,

$$\frac{1}{f_{rel}} = \left[\frac{2}{f_g} - \frac{t}{{f_g}^2}\right]$$

Solving for the group focal length gives

$$f_g = \sqrt{f_{rel} * (f_{rel} - t)} + f_{rel}$$

Examination of the above equation shows that the separation cannot exceed the relay focal length. While this holds true for thin lenses, a real lens can have a principal plane located outside of its physical dimensions as in the optimized design. As a starting point, picking intragroup spacing of 20 mm yields a group focal length of 25.6 mm. This provides a paraxial solution that satisfies both 1:1 imaging from the telescope focal plane to the detector, as well as the re-imaging of the telescope entrance pupil onto the cold stop.

For each group, doublets of germanium and silicon were used as a first-order solution. Constraints were placed on element powers, specifically their ratios, based on the desire for an athermalized system across a large temperature range. Since any lens barrel material can yield an athermalized doublet[18], aluminum was chosen to simplify the machining process.

First, the thermo-optical coefficients of germanium and silicon were calculated. These materials were chosen for availability across vendors, high radiation tolerance[19], and compatibility with diamond turning as well as deterministic polishing techniques. The thermal glass constant of a material is given by

$$\tau = \frac{dn/dT}{n-1} - \alpha,$$

With $\tau_{Si} = \frac{150\ ppm}{3.425-1} - 2.6\ ppm = 59.26\ ppm$, and $\tau_{Ge} = \frac{396\ ppm}{4.025-1} - 5.7\ ppm = 125.2\ ppm$

For an optically athermalized doublet in a lens barrel with coefficient of thermal expansion α_h, the following relations must be maintained[18]

$$f_A = \frac{(\tau_B - \tau_A)}{(\tau_B + \alpha_h)} f \quad , \quad f_B = \frac{(\tau_A - \tau_B)}{(\tau_A + \alpha_h)} f$$

Since the exact focal length of the groups is not of concern, a ratio of individual group elements was maintained instead of relating them to a fixed group focal length. With an aluminum lens barrel (α_h = 24 ppm), this ratio of element focal lengths is

$$f_{Ge}/f_{Si} = -\frac{(\tau_{Si} + \alpha_h)}{(\tau_{Ge} + \alpha_h)} = -\frac{59.26 + 24}{125.2 + 24} = -0.5573$$

The prescription for the optimized design is given, including the transmissive IDCA elements (relay elements are shaded for clarity). A full-system spot diagram is also presented over the operating temperature range. While the doublets were designed for a single wavelength, no additional steps was necessary for an achromatic system. Telescope aberrations are well corrected, and the asymmetric glass order used was found to have minimal chromatic aberration.

Relay/ IDCA Prescription

Surface	Material	Radius	Thickness
1	Germanium	-163.883	2.000
2		253.866	2.500
3	Silicon	121.002	3.500
4	(Asphere)	-39.626	10.000
5	Silicon	-	1.000
6	*Filter*	-	10.000
7	Germanium	37.193	1.800
8		22.503	1.350
9	Silicon	28.634	3.500
10		-	4.310
11	Germanium	-	1.016
12	*IDCA Window*	-	1.500
13	Sapphire	-	0.508
14	*Cold Filter*	-	18.938

Spot Diagram Over Temperature

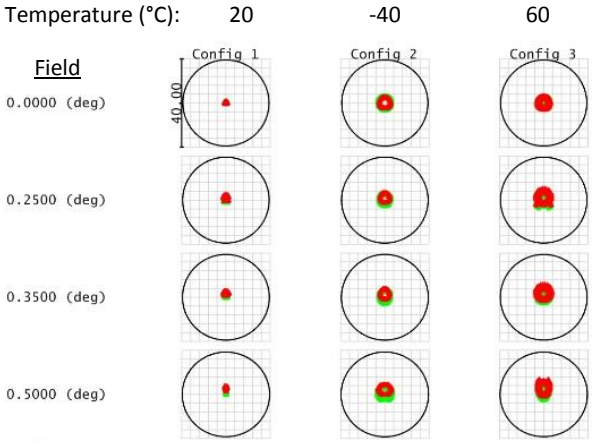

Airy Disk shown for λ = 4.0 µm, 19.5 µm radius

The collimator group which includes an aspheric surface and provides most of the image correction, drifted from the ideal power ratio computed above during software optimization, with a final value equal to -0.492. The ratio was more easily maintained on the camera group, which only has to correct for the color effects introduced by the

collimator. This is reflected in the higher temperature dependence of the collimator given in the table below; while each element changes significantly, the camera group EFL stays fixed due passive thermal compensation of the housing. Even with some temperature dependence of the collimator EFL, very little change is seen in relay EFL or magnification.

	20 deg. C	**-40 deg. C**		**60 deg. C**	
Element 1 FL	-32.19 mm	-32.45 mm	0.80%	-32.02 mm	-0.52%
Element 2 FL	15.80 mm	15.86 mm	0.37%	15.76 mm	-0.25%
Collimator EFL	25.61 mm	25.65 mm	0.17%	25.58 mm	-0.11%
Element 3 FL	-21.13 mm	-21.30 mm	0.77%	-21.03 mm	-0.51%
Element 4 FL	11.92 mm	11.96 mm	0.37%	11.88 mm	-0.25%
Camera EFL	25.69 mm	25.69 mm	0.00%	26.70 mm	0.00%
Relay EFL	21.268 mm	21.261 mm	-0.03%	21.273 mm	0.02%
Magnification	1.000	-1.001		-0.999	

Approximately 50 µm of residual thermal defocus remains due to the slight temperature dependence of the collimator focal length. This is well within the depth of focus of the system, but to minimize the design residual for wavefront error budgeting, a passive optomechanical athermalization was employed. Using a metering bracket composed of two materials, Invar and aluminum, and choosing a transition point to precisely tune the thermal growth of the bracket. This transition point was calculated by hand, and then optimized. This sets an effective CTE of the metering bracket to cancel out the residual defocus. It is assumed in the current model that all thermal growth and contraction manifests as piston, as the detailed optomechanical design is still underway. Future work will include fully modelling thermal effects of the finalized interfaces, identifying all possible deflection modes at the lens planes, and incorporating those results back into the optical analysis and error budget.

Part III: Design Study and Manufacture Assessment

A. Telescope Design Analysis

A custom design and fabrication of a MWIR instrument is a new undertaking for PRI, and a thorough assessment of manufacture feasibility was undertaken. Alignment tolerances being examined in detail, and continued discussions with component vendors has led to a comprehensive model of manufacture variances. The most critical single tolerance arises from the double bounce of the flat mirror, where a very strict stability requirement was identified. This sensitivity can be derived analytically, and was confirmed through system-level tolerance sensitivity and Monte Carlo simulations.

df/dS = f/(f1 – f2 – S) – 2 ; first term is usual separation error, second term due to fold-BFL distance.
Charles: I don't think this eqn is right, or maybe I'm just messing up the signs. I am going to ask Matt for help on this, out of interest if nothing else. Wish I could have gotten this in time!

While the front end is a zero-CTE, some uncertainty still exists due to residual thermal expansion and outgassing contraction in the carbon tube, as well as bracket material expansion. The impact of these effects must be kept within the stability requirement of the flat mirror, at +/- 4 µm, corresponding to a focal shift of -/+ 100 µm which is outside the depth of field[18]. This has driven a flexure based design for the flat cell that maintains z-position over temperature range, with expansion and contraction of the flexures resulting in a rotational motion.

As noted previously, an interesting consequence of the monolith design is turning typical alignment tolerances in a two-mirror telescope, i.e. positioning the secondary to the primary, into manufacturing tolerances. Because of this, a full-system interferogram will be provided by the monolith vendor using a properly aligned test flat. This ensures

the built-in system performance meets specifications, since it cannot be corrected if surface figure or coaxiality tolerances were to exceed the prescribed bounds.

Additionally, any significant power induced on the flat mirror, due to bending or thermal gradients, will be catastrophic to performance. An induced power of approximately $2.0*10^{-5}$ diopters is enough to degrade image performance beyond the diffraction limit, given an otherwise nominally focused instrument. Constructing the flat mirror from Zerodur, as with the primary/secondary monolith, will minimize the possibility of thermally induced bending. Finite element analysis will take place in coming months to quantify the expected amount of bending, but ultimately this will be de-risked by methods of in-lab testing and development of necessary mitigations such as thermal shielding.

B. Relay Design Analysis

Feasibility studies started with a tolerance analysis using a vendor's baseline precision grade tolerances[21]. In order to accurately model the system focus procedure, the telescope is focused using an on-axis spot size merit function and a three-axis compensation on the flat, followed by a full-field merit function for IDCA focus. The relay design underwent a typical cycle of tolerance allocation[22,23], but few major revisions were necessary. Element wedge and asphere irregularity rose to the top of the tolerance sensitivities, and both are at or near manufacture-limited precision.

Wavefront Error Budget

System Allowable WFE Requirement			**0.07518**
Design WFE			**0.00586**
System RSS WFE			**0.05613**
Front-End			**0.02004**
	Primary Mirror		**0.000008**
	Secondary Mirror		**0.003838**
	Flat Alignment		**0.019667**
Back End (Relay Lens & Filter)			**0.03884**
	Subsystem Alignment		**0.001820**
	Lens 1	**(Germanium, Bi-Concave, EFL = -32.8 mm)**	**0.009706**
		Manufacture	**0.003124**
		Alignment	**0.009190**
	Lens 2	**(Silicon, Bi-Convex Asphere, EFL = 15.9 mm)**	**0.025206**
		Manufacture	**0.021392**
		Alignment	**0.013331**
	Filter	**(Silicon, 1 mm Substrate)**	**0.010773**
		Manufacture	**0.010381**
		Alignment	**0.002880**
	Lens 3	**(Germanium, Meniscus, EFL = -20.7 mm)**	**0.018243**
		Manufacture	**0.017745**
		Alignment	**0.004233**
	Lens 4	**(Silicon, Convex-Plano, EFL = 11.8 mm)**	**0.018070**
		Manufacture	**0.013622**
		Alignment	**0.011873**
IDCA			**0.024864**

Units are waves of WFE, averaged over 9 equal-area field points and 3, 4, 5 µm wavelength. Flat stability in piston is by far the most sensitive item. Asphere irregularity, and wedge are the major contributions to error for the relay. The IDCA portion of the budget is based on conservative estimates for window and filter wedge, irregularity, etc. The full wavefront error budget is included as a separate document, and can be expanded to show more detail.

Cold stop efficiency was examined in detail, with results presented in the table below. A shearing of the reimaged exit pupil at the cold stop can be seen in the accompanying footprint diagrams. This is due to some natural curvature of the Gregorian pupil, and a lens design driven by correction at the image plane. Further design work for the flight prototype may include flattening the field, and reducing geometric distortion for the pupil/ cold stop conjugates to increase throughput for extreme field angles.

Vingetting vs. Field Height

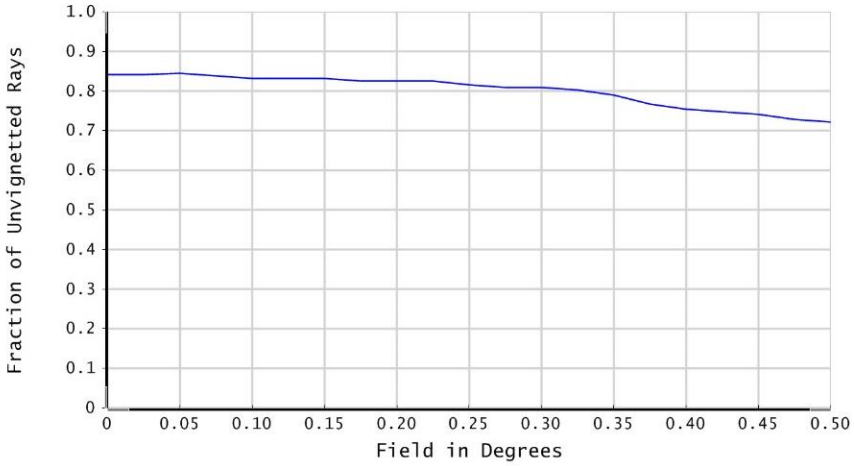

Above: The vingetting plot at the image plane shows a roll-off of relative illumination at the edges of the field.

Right: Footprint diagrams at the cold stop for 0 degree and 0.5 degree fields. Reduced cold stop efficiency as a function of field position is explained by a slight displacement of the telescope pupil imaged at the cold stop. Ray throughput includes losses to the central obscuration from the telescope.

Footprint Diagrams

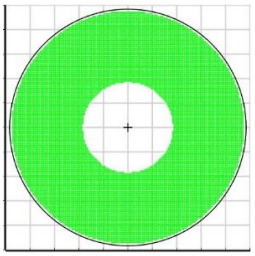

At 0 degree field,
84.2% rays through

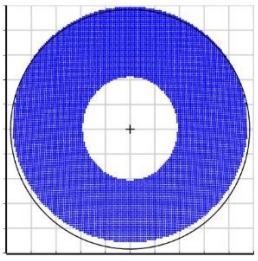

At 0.5 degree field,
70.3% rays through

A trade study was performed on the various compensations schemes, with both coarse (e.g., shimmed) and fine (mechanically actuated) adjustments taken as possibilities. The brute-force choice was to have a focus mechanism at the collimator group of the relay, to adjust for BFL variation, and a final focus mechanism at the IDCA. Due to the monolith thickness and telescope-relay interface architecture, a mechanism at that location proved to be challenging from an accessibility standpoint. Conveniently, the relay has a well-corrected image side conjugate for a wide range of object plane locations. Because of this, coarse focus at the intermediate telescope focus with a fine adjustment at the IDCA is sufficient.

The final compensation scheme includes fine adjustment in piston and tilt at the flat mirror, a shimmed interface at the telescope BFL, and fine adjustment at the IDCA. Shim thickness will be determined based on acceptance data from the monolith vendor, which will include the measured focal plane during system alignment. Mechanical tolerances are expected to suffice for angular alignment, and precise tilt adjustment at this interface can be incorporated later if deemed necessary. This is a simple solution that moves as little mass as possible, and is easily accessed during system integration.

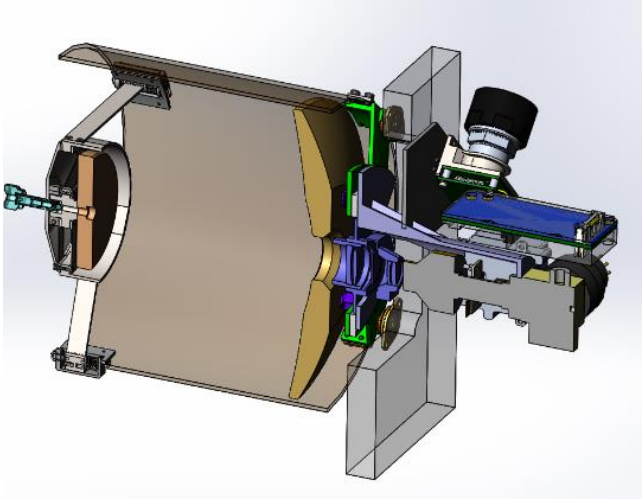

Cutaway model of the assembled instrument, including telescope tube and optical bench. Two of three total arms of the flat cell flexure are shown. The lack of working room between the telescope monolith and relay assembly is apparent, highlighting the benefit of a single actuated focus mechanism at the IDCA, rear of the relay.

Part IV: Implementation & Test Plan

A. Alignment & Image Performance

The telescope will be focused using visible light and a micro high definition camera, which affords much greater spot size resolution than focusing in the MWIR. Not only is there a reduction in the diffraction-limited spot size, which obscures aberrations, sampling can be increased by using a much smaller pixel pitch than the 15 µm of the IDCA. Below are image simulations at the telescope focal plane of 550 nanometer light on a 2.2 pixel pitch detector, compared to 4.0 micron light imaged onto 15 micron pixels. An angular displacement of one arcminute was introduced, equal to the tolerance bound.

Telescope Sampled Spot Size

λ = 4.0 µm, p = 15 µm	λ = 550 nm, p = 2.2 µm
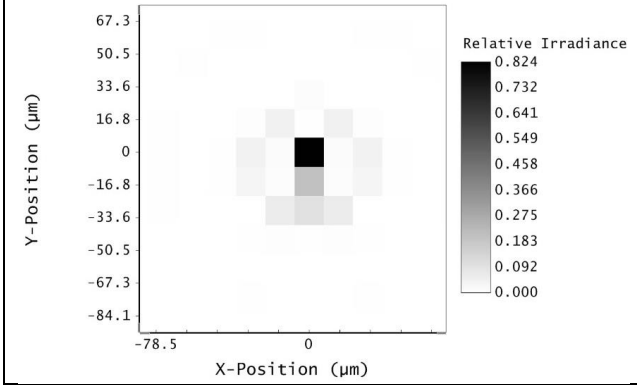	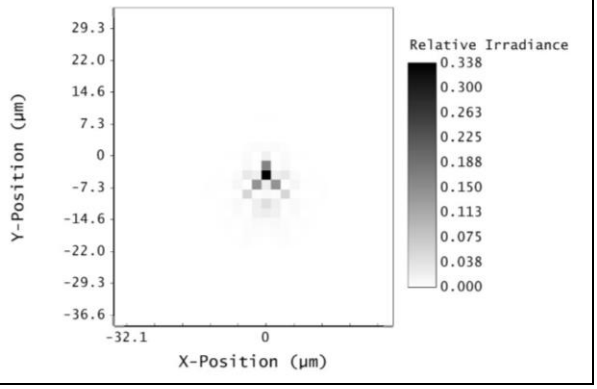

The presence of coma indicates a tilt of the flat mirror, and the direction of the tilt is more readily determined by the shape of the 550 nm PSF, as sampled by the 2.2 µm pitch detector. Rotational adjustments will be made to the flat to null the comatic aberrations, followed by a through-focus using piston adjustment. These adjustments will be iterated until an optimal focus is found, and the location of the focal plane to a telescope datum recorded. The relay lens assembly will be focused in a separate procedure, using a thermal source or other MWIR light source, while imaging on to the IDCA.

A MWIR interferometer is slated for instrument testing, but will not be available for prototype testing. Lacking this equipment, direct measurement of system-level wavefront error will not be possible. Diffraction limited performance is a fundamental property and can be measured in a number of ways, including modulation transfer function (MTF) testing. MTF tests will be used for system-level focus, performance testing, and at various intervals throughout environmental testing. For the A6 instrument, an MTF was measured and compared to lens vendor data to validate focus. A collimator was constructed using a full (on-axis) 10" parabola, precision flat of equal diameter, and fold mirror. Because of the reflective collimator design, broadband thermal sources can be used without issue, and can be focuses using visible portion of their emission. This will allow for full-aperture focusing and testing of the A100 instrument, and has already been used to validate focus of the A6 instrument (200 mm focal length, 50 mm entrance pupil), and a lens MTF was generated that closely matches that provided by the vendor.

Through the A6 instrument test process, a great deal was learned about successfully acquiring MWIR measurements. A well-characterized IDCA, more uniform thermal sources, and lessons learned in data processing will all improve A100 testing capabilities. Image acquisition follows the tilted slit method[24,25] which was found to provide the most reliable data with minimal setup time. Refinements have been made to test procedures and automated software developed to aid in noise reduction. This allows for full sampling of the optical MTF, even with the limitations of an undersampled detector, using sub-pixel registration algorithms. Alternative targets are also under investigation, including thermal targets of subpixel width wire arrays (*Holst). This could give secondary data points at discrete frequencies, to be checked against tilted slit method, as well as facilitate minimum resolved temperature difference testing.

B. Environmental Testing

The instrument will undergo thermal vacuum (TVAC) testing for survivability, for which PRI is well-equipped. The prototype instrument will undergo several cycles of the non-operational temperature range, as well as functional tests of the IDCA electronics and compute elements associated with imaging and cryocooler operation. PRI developed a custom digital board and that was tested in this fashion for the A6 instrument, and an upgraded version with high-speed readout is planned for the prototype.

Quantifying imaging performance under thermal environments poses a greater challenge. Thermal modelling will be done to assess the impact of vacuum conditions, and some empirical information can be acquired using thermocouple arrays while in TVAC. If gradients are deemed to be minimal, image testing across operating temperatures may be done at atmospheric pressure in a nitrogen purged environment. If vacuum significantly increases gradients, it is likely that image testing at vacuum will be needed –requiring a TVAC chamber upgrade or external facility. TVAC chamber upgrades, as well as external facilities, are both being pursued currently.

Component radiation hardness will be tested via total irradiated dose (TID) to gauge material sensitivity. The IDCA has already been validated by irradiation dosing at a local facility, followed by functional testing at PRI. Although the lens materials are single-crystal, and expected to be insensitive to radiation[19], any multilayer coatings used must be verified in a radiation environment. Similar to IDCA component testing, components will be irradiated at an external facility with in-house tests conducted prior to and after the irradiation. An appropriate monochrometer for transmission testing in the MWIR is currently being scoped.

Finally, in order to satisfy most secondary payload requirements, the assembled instrument must pass a contaminant test in a TVAC environment using a quartz crystal microbalance. Epoxies and potting materials used in the lens assembly, optical paints, and foreign debris introduced during assembly pose a risk to primary payloads. This will be a necessary validation step.The A6 instrument and spacecraft underwent similar testing earlier this year, and qualified well below acceptable contamination levels.

C. Calibration

Since fall of 2015, Planetary has been conducting aerial flight testing with a MWIR instrument using the same IDCA as A6 flight and A100 prototype instruments. This test campaign is informing the needed calibration procedure to acquire confident relative temperature data over long timespans. For summer 2016, the flight team will revisit the same field sites in eastern Washington where data partners in the agricultural business have been established. A ground sensor network is deployed along the flight paths, in addition to manual collection of temperature readings. Temperature calibrations will take place before and after each flight, using a Santa Barbra Infrared blackbody for temperature calibration and a liquid nitrogen-cooled target for background subtraction. Single-point flat field images are also taken immediately before takeoff for each flight to capture detector responsivity drift on the shortest timescale possible.

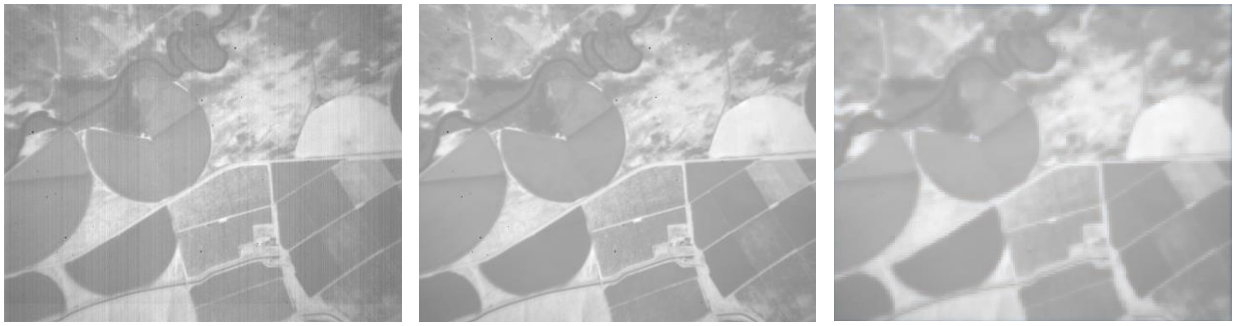

Left: Aerial campaign image, raw digital number (DN) count. *Middle:* Non-uniformity corrected DN count removes vertical striping and other artifacts. *Right:* Image simulation of the same area, using prototype instrument model and notional orbit parameters. For the simulation, the aerial image was centered about a 0.35 degree field point, and represents only a portion of the actual FOV from orbit. (View in PDF for best resolution)

Leveraging a growing expertise in image and data analysis, a radiometric calibration procedure is expected to be fully developed by the time the prototype A100 instrument is ready for testing. There is flexible space within the optical path to incorporate an onboard calibrator, which is slated for future design. To maximize the calibrator emissivity, thermal conductivity, and general bling factor, diamond substrate deposited with Vantablack[26] coating is under consideration. The design requirements of this calibrator (e.g. full vs. partial aperture, full vs. partial train), will be forthcoming based on a combination of aircraft flight testing, ground truth measurement, and in-lab calibration. Analysis of long-term trends aerial calibration data will inform the onboard calibration architecture for the constellation.

Part V: Conclusion

The internal design, assembly, and testing of a MWIR imaging system will be a significant step towards the earth observation goals of PRI. Providing a unique dataset will mean establishing new expertise in a number of areas; fortunately this has been bolstered by key partners in markets such as precision agriculture. Instrument development is a fundamental part of this plan, as it is unlikely that outsourcing production would be nearly as cost-effective at the volume needed for weekly revisit rates.

The ability to execute this prototype has been will be dependent on continued relationships with vendors, and communication between mechanical, optical and sensor characterization teams. Answering critical questions and retiring risks as early as possible will be a requirement for success in the burgeoning industry of satellite imagery. The test program for the prototype instrument is likely to generate new understanding as well as new questions, and improvements are expected before a flight instrument comes to fruition.

References

1. "Earth Observation." *Planetary Resources*. Web. 30 July 2016.
2. Mycroft, Frank "Planetary Resources, Inc." *Harvard Business Review*
3. Rivkin, A. S., H. Campins, J. P. Emery, E. S. Howell, J. Licandro, D. Takir, and F. Vilas. "Astronomical Observations of Volatiles on Asteroids." *Asteroids IV* (2015)
4. "About." Cubesat. Web. 20 July 2016. http://www.cubesat.org/about/
5. "SmallSat Deployment." *Nanoracks*. Web. 24 July 2016 http://nanoracks.com/products/smallsat-deployment/
6. "CubesSat Deployers" *ISIS*. Web. 24 July 2016. http://www.isispace.nl/product-category/satellite-products/cubesat-deployers/
7. "Sherpa." *Space Flight*. Web. 24 July 2016 http://www.spaceflight.com/sherpa/
8. "CubeSat Database." Micheal Swartwout. https://sites.google.com/a/slu.edu/swartwout/home/cubesat-database
9. Cochrane, Andy, Kevin Schulz, Rick Kendrick, and Ray Bell. "Q Selection for an Electro-optical Earth Imaging System: Theoretical and Experimental Results." *Opt. Express Optics Express* 21.19 (2013): 22124.
10. Fiete, Robert D. "Image Quality and λFN/p for Remote Sensing Systems." *Optical Engineering Opt. Eng* 38.7 (1999): 1229-40.
11. Tantalo, Theodore. "Comparison of SNR Image Quality Metrics for Remote Sensing Systems." *Optical Engineering Opt. Eng* 40.4 (2001): 574-85.
12. Lightsey, Paul A. "James Webb Space Telescope (JWST): Optical Performance of a Large Deployable Cryogenic Telescope." Cleo: 2014 (2014)
13. "6.2 Spatial Characteristics." *Landsat 7 Handbook*. N.p., 11 Mar. 2011. Web. 25 July 2016.
14. Riedl, Max J. "Comments and Guidelines for Selecting IR Objectives for Focal Plane Arrays." *Systems-Oriented Optical Design* (1993): 2-10.
15. "GEVS." NASA Technical Standards System. GSFC-STD-7000.
16. Wetherell, W. B., and M. P. Rimmer. "General Analysis of Aplanatic Cassegrain, Gregorian, and Schwarzschild Telescopes." *Appl. Opt. Applied Optics* 11.12 (1972): 2817-32.
17. Draganov, Vladimir, and Daryl G. James. "Compact Telescope for Free-space Communications." *Current Developments in Lens Design and Optical Engineering III* (2002)
18. Riedl, Max J. Optical Design Fundamentals for Infrared Systems. Bellingham, WA: SPIE, 2001.
19. Henson, Tammy D., and Geoffrey K. Torrington. "Space Radiation Testing of Radiation-resistant Glasses and Crystals." *Inorganic Optical Materials III* (2001)
20. "Classical two-mirror telescopes." *Telescope Optics.* Vladimir Sacek. Web. 27 July 2016. http://www.telescope-optics.net/classical_and_aplanatic.htm
21. "Optical Manufacturing Tolerance Chart." *Optimax Systems*. Web. 28 July 2016.
22. Ginsberg, Robert H. "Outline Of Tolerancing (From Performance Specification To Toleranced Drawings)." *Optical Engineering Opt. Eng* 20.2 (1981): 175-80.
23. Magarill, Simon. "Optomechanical Sensitivity and Tolerancing." *Optomechanical Engineering and Vibration Control* (1999): 220.
24. Mooney, Jonathan M. "Measurement of the Modulation Transfer Function of Infrared Cameras." *Optical Engineering Opt. Eng* 34.6 (1995): 1808.
25. Holst, Gerald C. *Testing and Evaluation of Infrared Imaging Systems*. Winter Park, FL: JCD Pub., 1998.
26. "Vantablack." *Surrey Nanosystems*. Web. 15 July 2016.